

ORIGINAL RESEARCH

Open Access



Zn/Fe bimetallic modified *Spartina alterniflora*-derived biochar heterostructure with superior catalytic performance for the degradation of malachite green

Hua Jing¹, Lili Ji^{2*}, Zilong Li^{1*}, Zhen Wang³, Ran Li² and Kaixuan Ju¹

Abstract

In this study, the synchronous magnetized carbonization method was utilized for preparing photocatalysis ZnO-Fe@SC heterostructure, which exhibited degradation efficiency 99.14% (60 min) for malachite green (200 mg/L) and could still maintain good performance after 5 cycles. The prepared ZnO-Fe@SC was analyzed using UV-Vis DRS, PL, SEM, TEM, BET, FTIR, XPS and VSM, and LC-MS for degradation products. The results indicate that photocatalyst has favorable magnetic properties, chemical stability and low charge carriers (e^-/h^+) recombination rate. The modification of bimetallics enables the composite photocatalyst to enhance the intensity of photogenerated electron transition. Moreover, quenching experiment revealed that the photo-generated holes (h^+) and superoxide radicals ($\cdot O_2^-$) were the dominant active species during the photocatalytic process, which degraded malachite green into small molecules by demethylation, deamination, ring-opening reactions as deduced from LC-MS analysis. ZnO-Fe@SC was prepared using a green, safe, low cost and operable synthetic method, which has a broad market potential in the field of environmental remediation.

Highlights

- ZnO-Fe@SC was prepared via simultaneous magnetized carbonization method using *Spartina alterniflora*-derived biochar.
- ZnO-Fe@SC was a heterojunction composite photocatalyst that could achieve up to 99.14% degradation performance of MG in 60 min.
- ZnO-Fe@SC could be effectively recycled to avoid the leaching of Nano-ZnO.

Keywords Bimetallic heterostructure, Nano-ZnO, Green synthesis, Photocatalytic degradation

Handling Editor: Yilai Lou

*Correspondence:

Lili Ji

jll-gb@163.com

Zilong Li

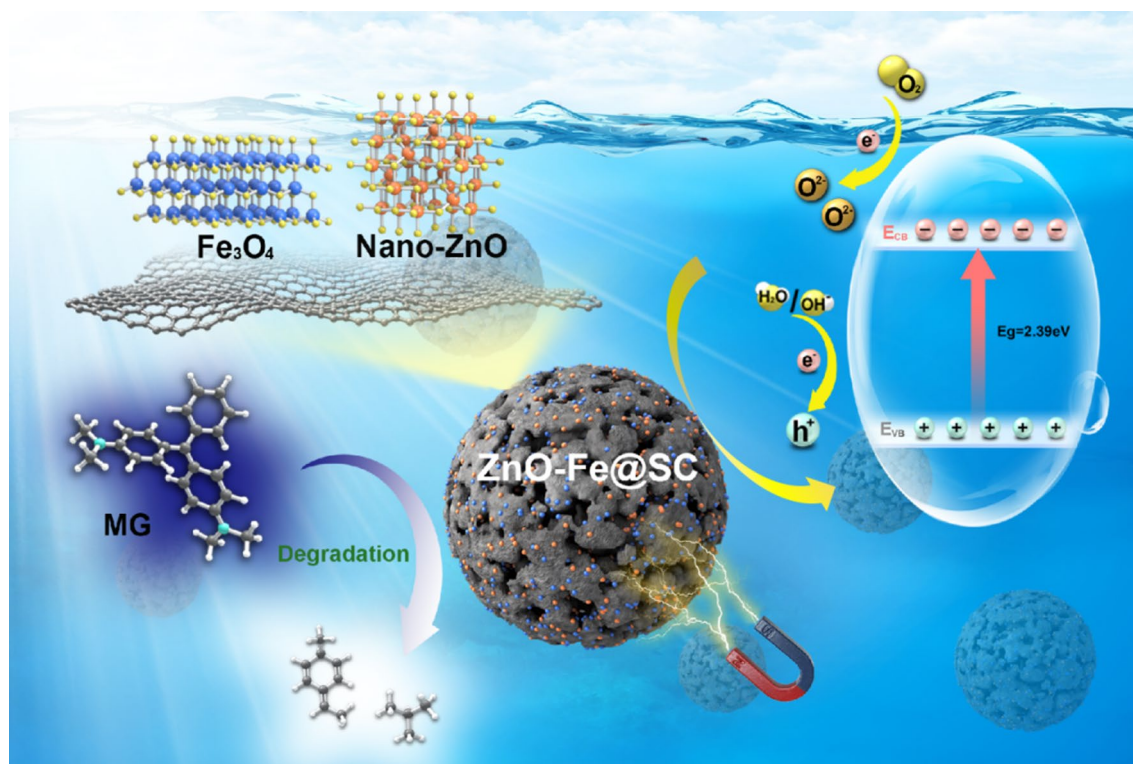
zilongli@zju.edu.cn

Full list of author information is available at the end of the article



© The Author(s) 2023. **Open Access** This article is licensed under a Creative Commons Attribution 4.0 International License, which permits use, sharing, adaptation, distribution and reproduction in any medium or format, as long as you give appropriate credit to the original author(s) and the source, provide a link to the Creative Commons licence, and indicate if changes were made. The images or other third party material in this article are included in the article's Creative Commons licence, unless indicated otherwise in a credit line to the material. If material is not included in the article's Creative Commons licence and your intended use is not permitted by statutory regulation or exceeds the permitted use, you will need to obtain permission directly from the copyright holder. To view a copy of this licence, visit <http://creativecommons.org/licenses/by/4.0/>.

Graphical Abstract



1 Introduction

Achieving carbon neutrality has become an important goal for several economies (Broadstock et al. 2021) and there is a need for exploring environmentally friendly materials. Among them, biochar has stimulated extensive research interest in environmental protection, energy conservation and combating climate change response. Additionally, several reports have demonstrated great potential of biochar for environmental remediation applications (Lawrinenko and Laird 2015; Huang et al. 2020; Ouakouak et al. 2021; Li et al. 2014). As a part of carbon family, it has a good electron transfer performance. Due to its low photoactivity, biochar reduces the photo corrosion rate (Otmane et al. 2022). In addition, biochar has a huge specific surface area (Chahinez et al. 2020), which is necessary for improving the photocatalytic performance of photocatalytic composites. Malachite green ($C_{23}H_{25}N_2Cl$, MG) is a commonly used water-soluble cationic dye in industry (Ledakowicz et al. 2021), and its antibacterial property makes it a widely used product in aquaculture and livestock breeding. MG has high cytotoxicity and can induce the formation of reactive

oxygen species (ROS), which can accumulate in the human body through ecological cycle and pose a serious threat to human health (Jiang et al. 2018). Extensive research has been conducted to develop methods for the elimination of organic dye pollutants. Among these different processes, advanced oxidation processes (AOPs) are gradually replacing the conventional methods with photocatalysis being a prominent technology (Liang et al. 2021). However, it is known that many semiconductor photocatalysts have some limitations, such as low degradation rate, rapid electron-hole recombination, difficult recovery and high cost, which greatly restrict their development and application in environmental remediation (Shao et al. 2019). Numerous modifications have been implemented to enhance photocatalytic activity of composite materials, such as surface modification, magnetization, and incorporation of bimetallic semiconductor nanoparticles. Recently, bimetallic nanoparticles (NPs) have received attention (Hosny et al. 2022). For example, the modification of biochar with iron-zinc bimetallic oxides (Fe-Zn) was reported with the goal of repairing tetracycline (TC) (Bhavani et al. 2018). Another report demonstrated

that Fe, Mo-embedded biochar catalysts can efficiently degrade organic contaminants (Yao et al. 2022).

ZnO has become a preferred material for semiconductor photocatalysis applications in addition to TiO₂. It is suitable for composite photocatalyst modification, because zinc-containing materials are considered as effective modifiers for improving pore structure and increasing surface area (Yang et al. 2021; Yu et al. 2020). Noei (2008) found that the specific surface area and total porosity of ZnO-modified biochar increased. However, ZnO has some disadvantages such as wide band gap, rapid electron-hole recombination and difficult recovery, which limit its application.

Magnetite and hematite are often used in the modification of composite materials (Zhang et al. 2020a, b). Magnetization of composite materials is usually carried out to append transition metal salts or other matter as magnetic precursors. This process is used to transform magnetic precursors into magnetic microparticles that are loaded onto carbon-based materials through heat treatment or physical and chemical reactions (Niu et al. 2020). Synthetic methods usually include impregnation-pyrolysis, chemical coprecipitation, solvothermal and reduction coprecipitation method (Nidheesh et al. 2021). Photocatalysts are generally prepared using expensive, complex and pollutive processes. Due to this, there has been more emphasis on raw materials that can be processed without toxic compounds using green synthesis approaches. As a magnetic precursor, potassium ferrate (K₂FeO₄) is often used for disinfection of drinking water since it is a clean material. As a green approach, the use of plants to synthesize Nano-ZnO has been widely studied. Some plants contain biologically active ingredients, especially flavonoids, which act as stabilizers, dispersants and reductants in the process of preparing Nano-ZnO. Due to these advantages, many plants have been reported to be successfully used to prepare Nano-ZnO, such as *centella asiatica* (Kumar et al. 2021), *orange fruit peel* (Thi et al. 2020), *Cassia fistula* and *Melia azedarach* (Naseer et al. 2020), *Acalypha indica* (Karthik et al. 2017), and so on.

Spartina alterniflora (*S. alterniflora*) is a typical salt marsh beach plant, which is an alien invasive species and poses a serious threat to the local ecosystem and economic development (Hedge et al. 2003; An et al. 2007). *S. alterniflora* plants have been shown to contain flavonoids, proteins, amino acids, alkaloids, and other useful substances. Hence, it is worth exploring the use of *S. alterniflora* plants to synthesize Nano-ZnO. To the best of our knowledge, the application and effect of *S. alterniflora*-derived biochar modified by Fe-Zn bimetal in remediation of organic polluted water has not been well explored.

In this study, the bimetallic modified *S. alterniflora* biochar composite photocatalyst (ZnO-Fe@SC) was prepared by simultaneous magnetized carbonization method to immobilize the iron oxide precursor and facilitate the uniform growth of nano-ZnO crystals on *S. alterniflora* biochar. The entire process was simple, safe, and pollution-free, which satisfied the requirements of green chemistry. The physicochemical properties of ZnO-Fe@SC were analyzed by X-ray diffraction (XRD), Fourier transform infrared spectroscopy (FTIR), scanning electron microscopy (SEM), transmission electron microscope (TEM), Raman spectroscopy, fluorescence emission spectroscopy (PL), X-ray photoelectron spectroscopy (XPS), UV-Vis diffuse reflectance spectrum (UV-Vis DRS) and vibrating specimen magnetometer (VSM). In addition, MG was used as the target degradation product to explore the degradation performance and mechanism of ZnO-Fe@SC.

2 Experimental section

2.1 Chemical reagents and materials

S. alterniflora was collected from Zhoushan, Zhejiang Province, China. It was cleaned with distilled water, dried overnight at 80 °C, and crushed into powder in a pulverizer (XDW-6 J Jinan China).

Zinc acetate dihydrate (C₄H₁₀O₆Zn), MG (C₂₃H₂₅ClN₂), polyvinylpyrrolidone ((C₆H₉NaOH)_n, K₃₀), sodium hydrate (NaOH), potassium ferrate (K₂FeO₄), dimethyl sulfoxide ((CH₃)₂SO), formic acid (HCOOH), and *p*-benzoquinone (C₆H₄O₂) were all purchased from Sinopharm Chemical Reagent Co., Ltd. All chemicals were of analytical grade and were applied without further treatment.

2.2 Preparation of *S. alterniflora* biochar

S. alterniflora powder was uniformly placed in a quartz crucible, carbonized in a tube furnace, and fed with nitrogen, under a flow velocity of 70 mL/min. The tube furnace was adjusted to 200 °C at a heating rate of 5 °C/min and maintained for half an hour. It was heated up to 800 °C at a rate of 5 °C/min, and maintained for 2 h. After pyrolysis, the temperature was reduced to 30 °C at a rate of 5 °C/min, at which point the nitrogen was stopped. The carbonized material was taken out and sieved (100 mesh) to obtain *S. alterniflora* biochar with 99.72% purity.

2.3 Synthesis of ZnO-Fe@SC

Four g of *S. alterniflora* was mixed with ethanol (400 mL, 95%) at 80 °C for 2 h. The supernatant was taken out, put into a beaker with zinc acetate dihydrate (1.756 g, 0.02 mol/L) along with a glass rod at a constant temperature, and stirred with a magnetic stirrer at 80 °C for 10 min. PVP (0.1 g, 0.0000625 mol/L) and NaOH (0.4 mol/L) were added into the supernatant mixture in

that order, and stirred for 2 h to form a milky green complex, which constituted the Nano-ZnO precursor. Then K_2FeO_4 was mixed with *S. alterniflora* biochar in a mass ratio of 1.98:1, which was added into Nano-ZnO precursor solution, stirred at 80 °C for 5 h, centrifuged at 6000 r/min for 2 min, and dried in an air oven at 80 °C overnight to obtain a solid powder.

The obtained solid powder was placed in a tube furnace to obtain a bimetallic modified *S. alterniflora* biochar composite photocatalyst (ZnO-Fe@SC) by high temperature anaerobic carbonization. The calcination conditions were identical to the ones used for preparing *S. alterniflora* biochar. As a control, the experimental steps were repeated to obtain ZnO@BC without adding K_2FeO_4 . Nano-ZnO was obtained by calcining Nano-ZnO precursor in an oxygen-free tube furnace at 400 °C for 120 min at a rate of 5 °C/min. The annealing and cooling rate was 5 °C/min.

2.4 Characterization techniques

XRD (MiniFlex600, Japan) was performed to determine the crystal phase composition in the scope of 2θ from 20° to 80°. FTIR (IRAffinity-1 S, Japan) was used to analyze the surface functional groups in the 4000–400 cm^{-1} region. UV-Vis DRS (UV 3600, Shimadzu, Japan) was applied to explore optical properties using $BaSO_4$ as a reference. The recombination frequency of the charge carriers was analyzed by PL (FLS980, England) at an excitation wavelength of 350 nm. SEM (Hitachi Su8010, Japan) and TEM (FEI Tecnai G2 F20 S-Twin, USA) were used to observe the morphology and microstructure of the surface. Elemental distribution was obtained by energy-dispersive spectrometry (EDS). Based on Brunauer-Emmett-Teller (BET) method, the specific surface area and pore size distribution of the prepared samples were evaluated. The surface chemical state and quantity were determined by XPS (Escalab 250Xi, USA). VSM (Lakeshore 7407, USA) was used to investigate the magnetic properties at 300 K.

2.5 Photodegradation of MG using ZnO-Fe@SC

The photocatalytic activity of ZnO-Fe@SC was evaluated by the degradation of MG aqueous solution in a photochemical reactor (PhchemIII, Beijing, China). ZnO@BC and Nano-ZnO were added as reference for carrying out parallel experiments. The prepared sample powder (0.04 g) was added to MG solution (100 mL, 200 mg/L), stirred for 60 min without light to establish equilibrium of absorption and desorption, and then illuminated for 1 h using a xenon lamp with a filter cut-off wavelength of 390 nm (FSX-300, NBeT Group Corp, Beijing). Aliquots (2 mL) were collected every 10 min and the solid photocatalyst was filtered out. Then, using UV-Vis

spectrometer (UV 3600, Shimadzu, Japan) the absorbance was measured at a wavelength of 617 nm, which corresponded to the absorption of MG. The photocatalytic degradation efficiency (D%) was calculated from Eq. (1). The photocatalytic degradation process was fitted by pseudo-first-order kinetic equation as expressed in Eq. (2).

$$D\% = \frac{C_0 - C}{C_0} \times 100\%, \quad (1)$$

$$-\ln \frac{C}{C_0} = kt, \quad (2)$$

where C_0 and C are the initial concentration of MG in aqueous solution and the concentration at time t , respectively, and k is the photocatalytic rate constant.

2.6 Radical scavenging experiment

One mL of p-benzoquinone (BQ, 0.1 mol/L), dimethyl sulfoxide (DMSO, 0.2 mol/L) and formic acid (FA, 0.2 mol/L) as scavengers for ($\cdot O_2^-$), ($\cdot OH$), and (h^+) were prepared. They were appended into the reaction solution to be degraded before the illumination so that active species involved in the photocatalytic reaction could be analyzed.

2.7 Magnetic recovery cycle experiment

The repeat cycle experiments performed to assess the stability of the ZnO-Fe@SC in degrading organic dyes. After each cycle was completed, the ZnO-Fe@SC powder was separated using an external magnetic field, washed with ethanol and then washed again with distilled water until neutral, and finally placed in an oven at 60 °C. The cycles of photocatalytic degradation and magnetic separation were carried out for 5 times.

2.8 Degradation products analysis

The MG degradation products using ZnO-Fe@SC were detected by electrospray ionization (ESI) positive ion mode liquid chromatography-mass spectrometry (LC-MS, 1290II-6460, Agilent, USA). Solution A was the mobile phase, which consisted of 0.1 M acetate and acetic acid (pH 5.3). Whereas solution B, which was the solution phase, consisted of acetonitrile at a flow rate of 0.2 mL/min and a column temperature of 40 °C. For EIS, the flow rate of the atomizing gas was set to 10 L/min. The pressure was set to 45 psi, and the monitored mass debris ranged from 10 m/z to 600 m/z .

3 Results

3.1 Analysis of chemical compositions

The crystal structure and phase analysis of biochar, Nano-ZnO, ZnO@BC, ZnO-Fe@SC were performed by

XRD as shown in Fig. 1a. Compared with Nano-ZnO, the peaks of ZnO-Fe@SC were found to be located at 31.70° , 34.40° , 36.18° , 47.53° and 56.84° , which were perfectly indexed to (100), (002), (101), (102), and (110) planes of ZnO (JCPDS 36-1451), respectively (Madhu et al. 2016). This indicated that the structure of the prepared ZnO crystals was not affected by the preparation process. Even though the characteristic peak of the ZnO was weakened, it still coexisted in ZnO-Fe@SC. Moreover, the peaks of ZnO-Fe@SC located at 29.98° , 35.34° , 42.96° , 56.84° , and 62.48° were indexed to the (220), (311), (400), (511), and (440) planes of Fe_3O_4 (JCPDS, 89-3854) (Yu et al. 2020). From these results it can be concluded that Fe ion was successfully loaded into ZnO@BC in the form of Fe_3O_4 , thus validating the successful synthesis of ZnO-Fe@SC.

In the FTIR spectra, the characteristic peak at $400\text{--}600\text{ cm}^{-1}$ is attributed to the Zn-O (Leichtweis et al. 2020), as shown in Fig. 1b. The peaks of ZnO-Fe@SC, ZnO@BC, Nano-ZnO in this region gradually decreased and exhibited a blue shift phenomenon, which may be related to the formation of the Fe-O bond and the interaction between biochar and ZnO during the preparation process. Meanwhile, the peaks at 1050 cm^{-1} in biochar are attributed to the aromatic C-O, which is blue shifted in ZnO-Fe@SC. The peak near 1391 cm^{-1} in ZnO-Fe@SC is ascribed to the phenolic O-H groups (Harini et al. 2020). In addition, the new band of ZnO-Fe@SC at 1629 cm^{-1} is related to the presence of carbonyl groups (Kamal et al. 2022), implying that the interaction between carbon material and ZnO particles is strengthened by further treatment. Furthermore, the peaks of Nano-ZnO, ZnO@BC and ZnO-Fe@SC around 3439 cm^{-1} are attributed to the O-H bond, where a decrease was observed in the intensity of the broad band.

The XPS survey spectrum of ZnO-Fe@SC mainly includes C, O, Fe and Zn, as shown in Additional file 1:

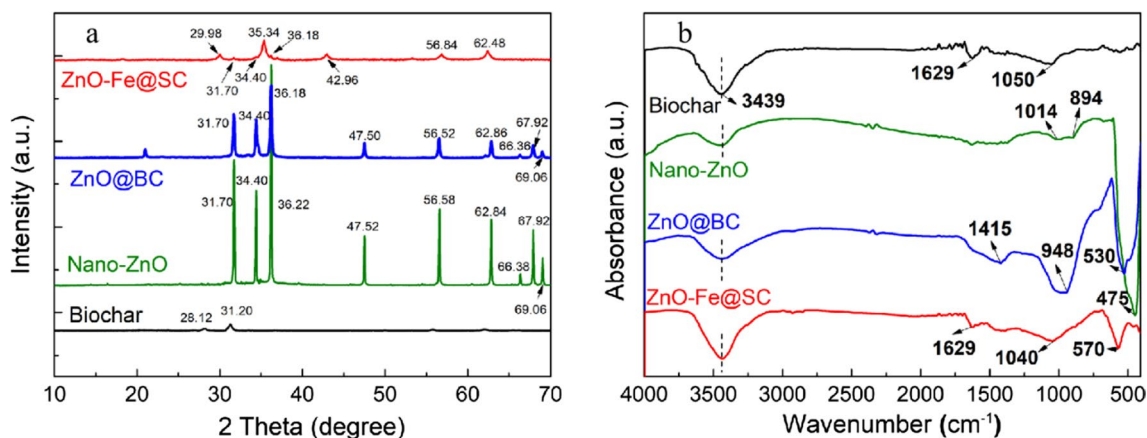


Fig. 1 a XRD patterns (a) and FTIR patterns (b) of Biochar, Nano-ZnO, ZnO@BC and ZnO-Fe@SC

Fig. S1. In Fe 2p spectrum (Fig. 2a), the binding energies at 711.88 eV and 725.38 eV correspond to Fe $2p_{3/2}$ and Fe $2p_{1/2}$, respectively (Du et al. 2018). The Fe 2p peak can be deconvoluted into four peaks, namely, Fe (III) (711.88 eV , 715.68 eV , 725.38 eV) and Fe (II) (719.38 eV) (Wan et al. 2017). This further indicates that Fe_3O_4 plays a ferromagnetic role in ZnO-Fe@SC, which is consistent with XRD analysis. The C 1s spectrum (Fig. 2b) located at 284.78 eV , 286.08 eV , and 289.01 eV correspond to C-C, C-O and C=O functional groups, respectively (Yan et al. 2020). From the Zn 2p spectrum (Fig. 2c), the Zn $2p_{1/2}$ and Zn $2p_{3/2}$ can be found to appear at 1045.48 eV and 1022.28 eV (Hu et al. 2020), indicating that the addition of Fe_3O_4 does not change the chemical properties of Nano-ZnO. In the O 1s spectrum (Fig. 2d), the peaks at 530.88 eV , 532.08 eV and 532.48 eV are attributed to O-H, C-O and C-O-ZnO bond, respectively (Song et al. 2020). In particular, the existence of C-O-Zn bond further proves the successful loading of Nano-ZnO onto biochar.

3.2 Optical properties

UV-Vis DRS spectra show that Nano-ZnO exhibited a maximum absorption edge at $388\text{--}390\text{ nm}$, which is consistent with the previous research results (Liu et al. 2019a, b), as shown in Fig. 3. The absorption spectra of ZnO-Fe@SC and ZnO@BC exhibited significant broadening owing to the influence of *S. alterniflora* biochar. The Tauc plot method is used to calculate the band gap energy of photocatalysts (Kaliraj et al. 2019), which provides theoretical support for the possible photocatalyst reaction mechanism. As shown in the Fig. 3b, the band-gap of ZnO-Fe@SC (2.39 eV) was reduced as compared to Nano-ZnO (3.18 eV). This is possible due to interaction of *S. alterniflora* biochar with the bimetal causing surface defect states and the formation of Zn-O-C

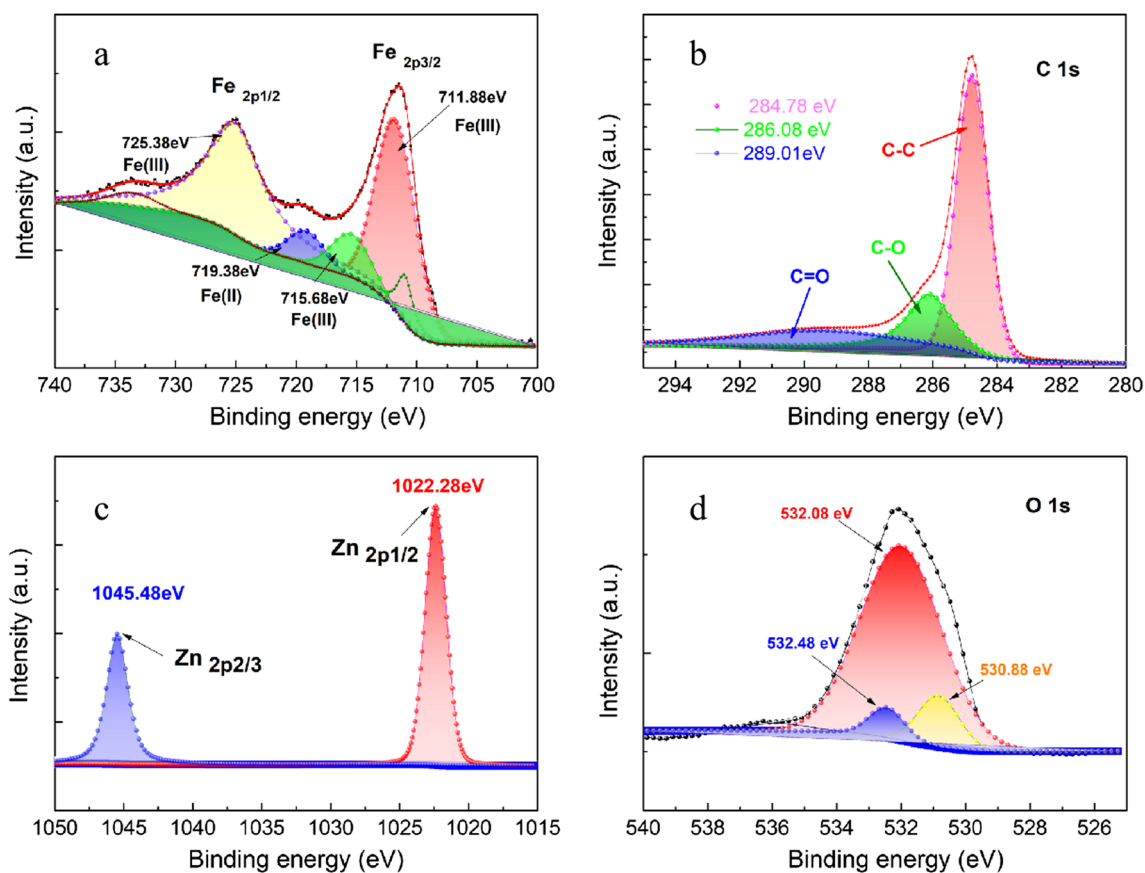


Fig. 2 XPS spectrum of ZnO-Fe@SC

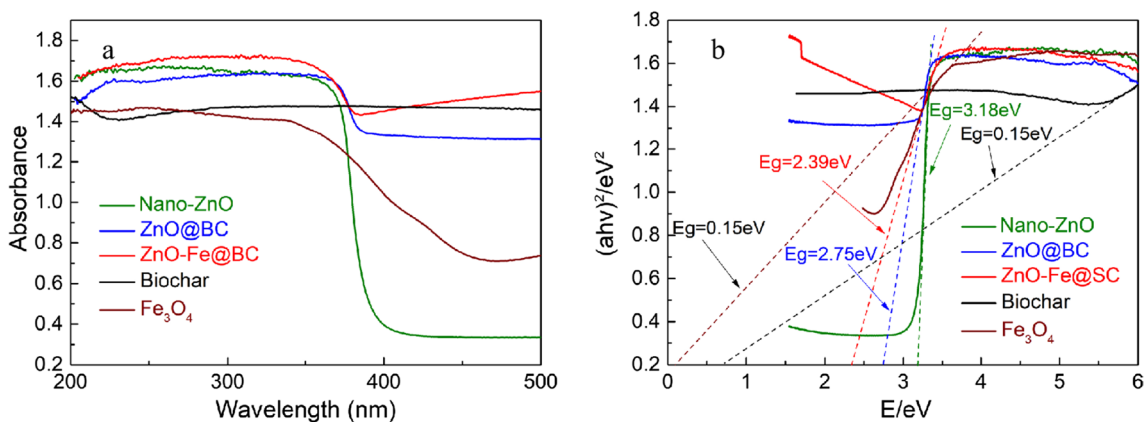


Fig. 3 UV-Vis spectra (a) and optical band gap energies (b) of Biochar, Fe₃O₄, Nano-ZnO, ZnO@BC and ZnO-Fe@SC

bonds within ZnO-Fe@SC (Samadi et al. 2012). During the photocatalytic process, electrons in the valence band of the catalyst are activated and transferred to the conduction band under the influence of light, thereby producing electron-hole pairs. Hence, the smaller bandgap of ZnO-Fe@SC is beneficial for enhancing the electron

transfer to generate radicals (Yao et al. 2015). Compared with ZnO@BC, the band gap energy of ZnO-Fe@SC was smaller, which indicates that the addition of Fe ion increased the ability of the photocatalyst to drive the photogenerated electron transition. Furthermore, it can be obtained by empirical equation (Chen et al. 2012)

that the E_{VB} potentials of Nano-ZnO and Fe_3O_4 were 2.89 and 1.38 eV, respectively. Whereas the E_{CB} potentials of Nano-ZnO and Fe_3O_4 were -0.29 and 1.23 eV, respectively.

The PL spectra revealed that the peak intensities of ZnO@BC and ZnO-Fe@SC significantly decreased as compared to the Nano-ZnO, as shown in Fig. 4. A lower PL intensity indicates that the modified composite has better charge separation and lower recombination rate of charge carriers, which is attributed to the presence of the *S. alterniflora* biochar. Additionally, the presence of an emission peak at about 468 nm of ZnO-Fe@SC is ascribed to the addition of Fe_3O_4 in the photocatalyst (Liu et al. 2019a, b).

3.3 Morphology and textural property

According to the classification of IUPAC, the adsorption of ZnO-Fe@SC followed a type IV isotherm, which indicates that the composite is a mesoporous adsorbent, as shown in Additional file 1: Fig. S2a. When the pressure p is less than the saturation pressure P_0 , the absorption is related to the filling of the micropores, and the isotherm has an upward convex trend. When $P/P_0 > 0.4$, an H4 type hysteresis loop is generated due to the metastable state of adsorption. This phenomenon indicates that ZnO-Fe@SC had a certain number of slit pores (Zhang et al. 2020b). H4 hysteresis loops usually exist in aggregated crystals of micro-mesoporous carbon, which is related to *S. alterniflora* biochar. The pore size distribution curve of ZnO-Fe@SC in Additional file 1: Fig. S2b indicates that the pore diameter ranged mostly of 10 and 40 nm. The pore volume of ZnO-Fe@SC was $0.120 \text{ cm}^3 \text{ g}^{-1}$ and the specific surface area was $215.82 \text{ m}^2/\text{g}$. ZnO-Fe@SC had a higher specific surface area mainly due to KOH produced by the carbonization of K_2FeO_4 in the precursor material. KOH can be used to activate the surface of *S. alterniflora* biochar to form pores. In addition, another reason why

ZnO-Fe@SC had a higher specific surface area may be the existence of an inter-particle area between ferromagnet particles located on biochar (Zubrik et al. 2022).

The surface morphology and microstructure of ZnO-Fe@SC were analyzed by SEM, TEM, as shown in Fig. 5. SEM images show that *S. alterniflora* biochar exhibited a porous structure, as shown in Fig. 5a. This is due to the removal of volatile substances during pyrolysis process (200°C for 30 min) and the role of KOH activator produced by K_2FeO_4 . The porous structure can support loading of Nano-ZnO and Fe_3O_4 , which assembles to form a heterostructure. A larger specific surface area and abundant pore structure can provide attachment and reaction sites to capture organic pollutant molecules. It can be seen from Fig. 5b, c that most of Fe_3O_4 grows in a disorderly rod-shaped manner on the surface of biochar. The sizes of Nano-ZnO particles were found to be in the range of 28–45 nm. Furthermore, Nano-ZnO exhibits a uniform 3D spherical structure and is well dispersed in the biochar carrier. This shows that the incorporation of the ferromagnetic ore does not affect the growth of Nano-ZnO during the synthesis process. Specially, the surface functional groups of *S. alterniflora* biochar can affect the crystal morphology of Nano-ZnO (Miao et al. 2017). The microscopic morphology of ZnO-Fe@SC obtained by high-resolution TEM (HRTEM) indicates the appearance of high-quality crystals with neat lattice fringes, as shown in Fig. 5(d–e). The presence of two distinct interlocking lattices of 0.260 nm and 0.253 nm, belonging to the ZnO crystal (002) and Fe_3O_4 crystal (311), respectively, confirms the formation of heterojunctions. In Fig. 5e, the *S. alterniflora* is mostly composed of amorphous carbon representing numerous frosted folds in the TEM images. Moreover, Nano-ZnO is well dispersed in *S. alterniflora* biochar with a near spherical shape, whereas Fe_3O_4 exhibits rod-like shapes, which is consistent with SEM images. Furthermore, the SAED pattern revealed the polycrystalline nature of the composite photocatalytic material, as shown in Fig. 5f. The EDS mapping demonstrated that C, Fe, Zn, and O, all exist in the photocatalyst and are evenly dispersed, as shown in Fig. 5g–k.

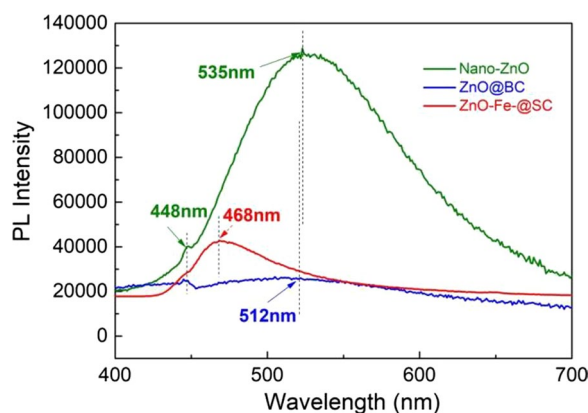


Fig. 4 PL spectra of Nano-ZnO, ZnO@BC and ZnO-Fe@SC

3.4 Photocatalytic degradation performance

The photocatalytic performance of ZnO-Fe@SC was assessed by applying it in the degradation of MG. Figure 6a shows that the introduction of ZnO-Fe@SC resulted in a faster degradation as compared to Nano-ZnO and ZnO@BC in the dark reaction. This is attributed to the larger pore volume and surface area of ZnO-Fe@SC. Under dark conditions, the main degradation pathway is adsorption, since the catalyst has no access to external energy. Under illumination, the concentration of

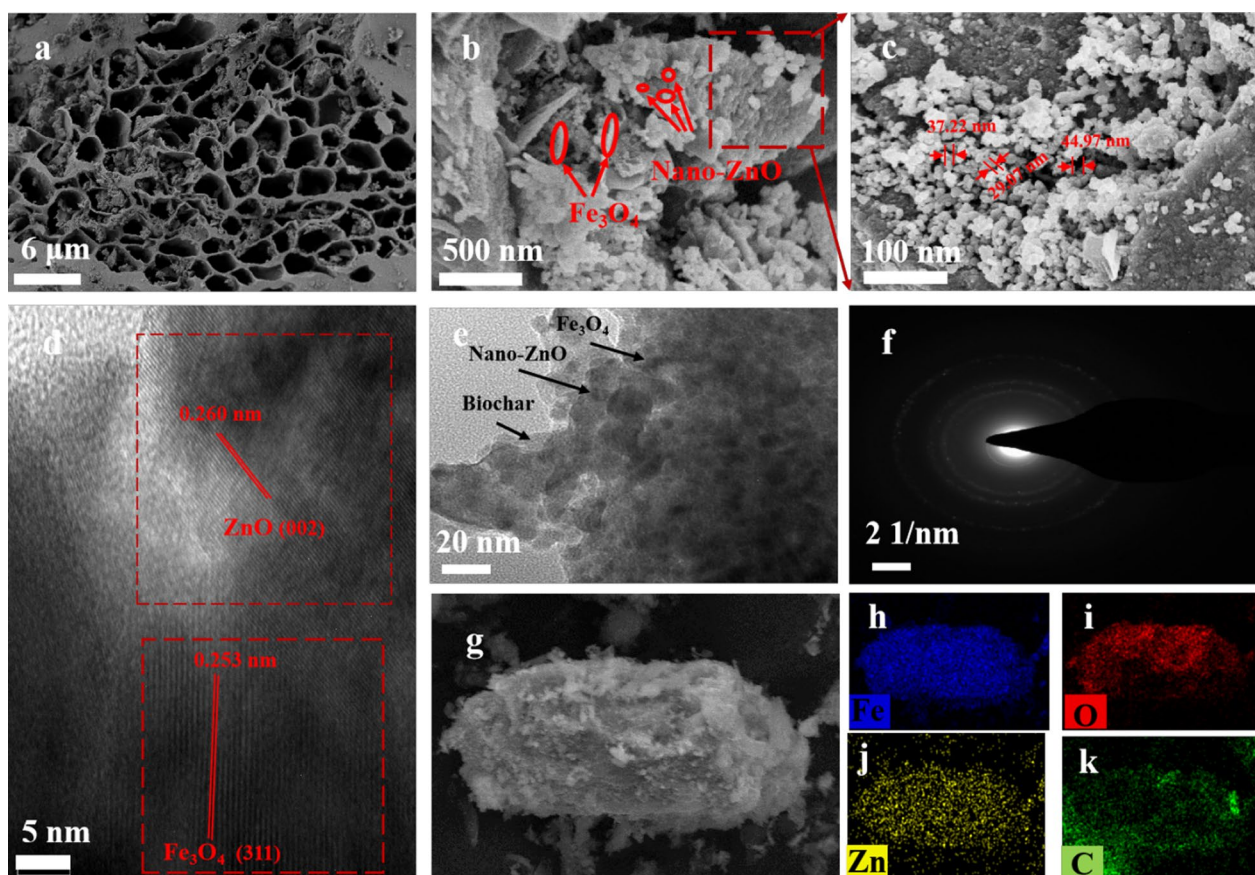


Fig. 5 FE-SEM images of ZnO-Fe@SC (a–c), the TEM (d–e), SAED pattern(n), and EDS mapping (g–k) of ZnO-Fe@SC

MG solution with ZnO-Fe@SC catalyst decreased faster than ZnO@BC, which may be related to the Fe_3O_4 . The addition of Fe ion in composite photocatalyst has shown to greatly improve the electron transfer ability (Eltaweil et al. 2020).

The total removal rate of MG using ZnO-Fe@SC was 99.14% after 1 h of illumination. Analysis of degradation performance of MG by different addition amounts of ZnO-Fe@SC (Fig. 6b) showed that the catalyst dosage of 0.05 g had a slightly higher photocatalytic degradation rate than 0.04 g with a 99% degradation rate of MG. High doses were not desirable due to shielding and light scattering effects, which can limit the utilization of light sources. In addition, the degradation rate increased when the addition amount was in the 0.02–0.04 g range. Figure 6c shows that the removal rate dropped to 91.27% when the MG concentration was 300 mg L^{-1} . This is mainly attributed to the rapid equilibration of active sites in ZnO-Fe@SC composites at high concentrations, which hinders the electron transfer in ZnO-Fe@SC. Further, the decrease of solution transmittance leads to the decrease in the MG removal efficiency. The time distribution of

the pseudo-first-order kinetic curve of photocatalytic degradation of MG (Fig. 6d) demonstrated that the photodegradation efficiency and reaction rate were related to the pseudo-first order kinetics. Particularly, the k value of ZnO-Fe@SC was higher than that of Nano-ZnO, showing high UV–Vis photocatalytic activity (Tang et al. 2018). In addition, from the UV–Vis spectra (Additional file 1: Fig. S3) it can be seen that the characteristic peak intensity of MG gradually decreases with the degradation process due to the photocatalytic degradation of ZnO-Fe@SC.

3.5 Radical scavenging experimental analyses

ROS trapping experiments can detect whether active substances participate in the degradation and also identify the involved ROS. As shown in Additional file 1: Fig. S4, the degradation efficiency of MG was significantly reduced when BQ and FA were added in the photocatalytic degradation process. The degradation rates were only 7.83% and 2.11% after 60 min of illumination. Introducing DMSO showed a slight effect on the degradation efficiency, indicating that photo-generated holes (h^+) and superoxide radicals ($\cdot\text{O}_2^-$) played

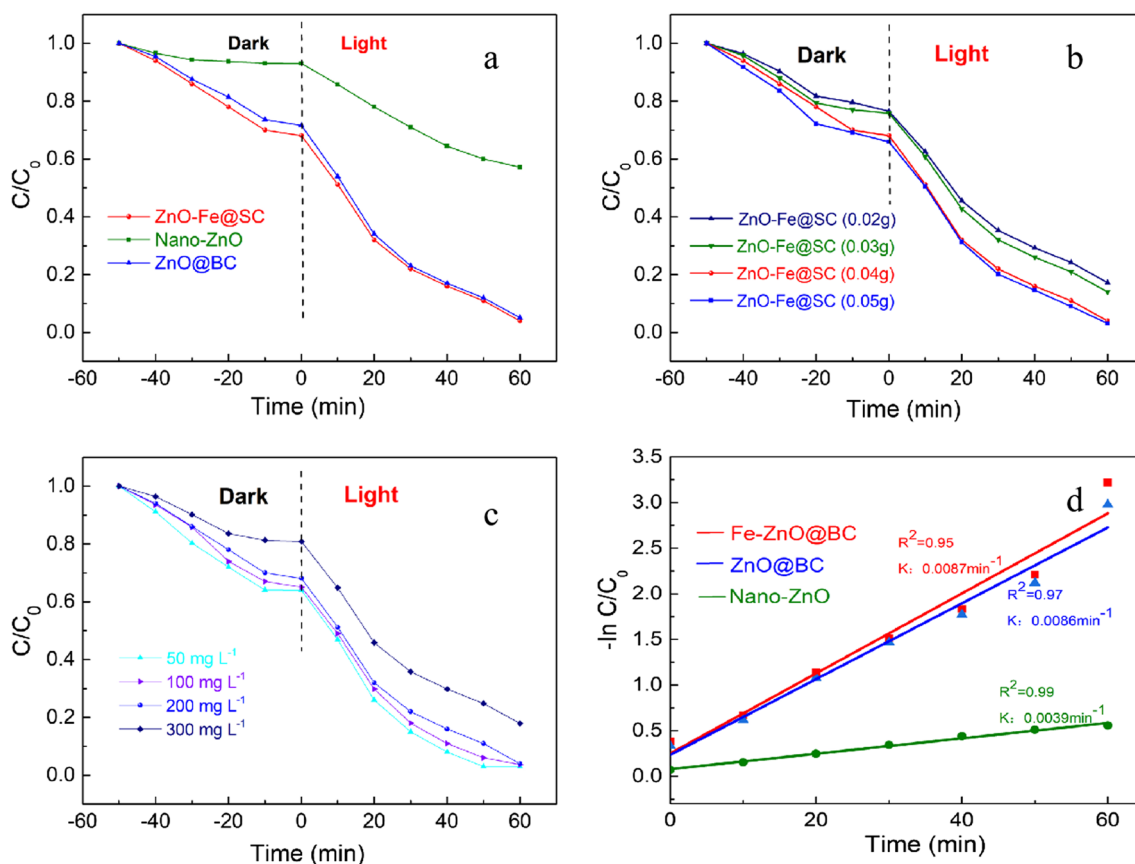


Fig. 6 **a** The removal rate of MG on Nano-ZnO, ZnO@BC and ZnO-Fe@SC under visible light irradiation. **b** Different dosage of ZnO-Fe@SC for the photocatalytic degradation of MG (200 mg/L). **c** Performance of ZnO-Fe@SC (0.4 mg/mL) for the photocatalytic degradation of MG under different concentrations. **d** First-order kinetics of ZnO-Fe@SC for photocatalytic degradation of MG

main roles in the degradation process, while $(\cdot\text{OH})$ hardly contributed in this experiment.

3.6 Magnetic recovery cycle experiment

As shown in Fig. 7a, the saturated magnetization (MS) of ZnO-Fe@SC reached up to $22.13 \text{ emu}\cdot\text{g}^{-1}$, exhibiting ferromagnetism. This phenomenon is attributed to the addition of K_2FeO_4 during the synthesis, which

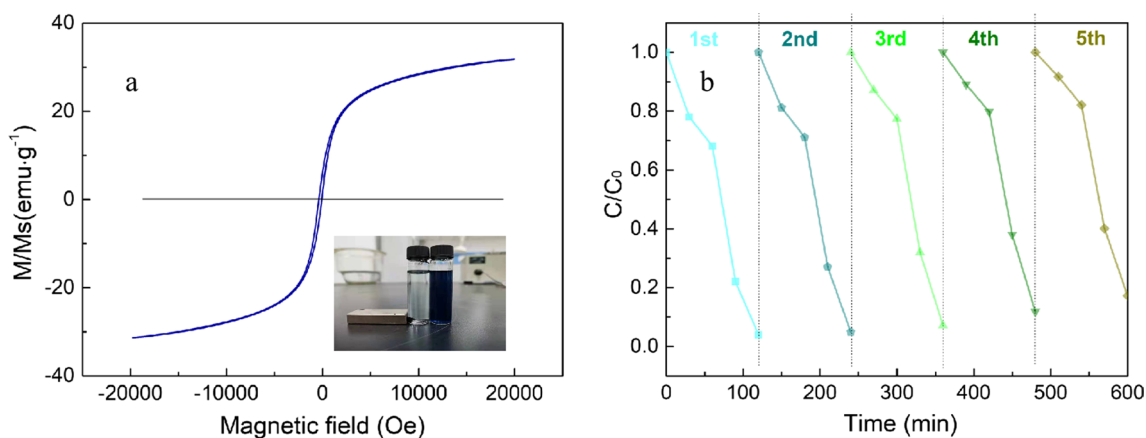
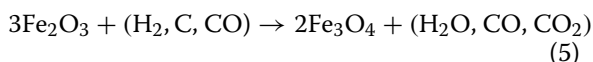
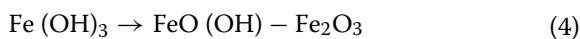


Fig. 7 **a** VSM spectrum of ZnO-Fe@SC. **b** Cycling experiments

is pyrolyzed into activator (K) and catalyst (Fe ions) at high temperatures. The reaction process is described as follows:



Meanwhile, Fe(OH)₃ is converted to Fe₃O₄ at high temperatures described as:



The excellent ferromagnetic properties of the synthesized ZnO-Fe@SC are beneficial to the separation of

composite photocatalysts from aqueous solutions. The degradation rate of MG by ZnO-Fe@SC remained above 98.50% after 5 cycles (Fig. 7b), indicating that ZnO-Fe@SC had excellent stability and reusability.

3.7 Analysis of degradation products

In the photocatalytic degradation experiments of MG using ZnO-Fe@SC, the decolorization rate of the end product of MG degradation reached 99.14%. However, the existence of MG leucocarbinol, which is the non-ionic colorless form of MG in aqueous solution, needs to be considered as well (Chen et al. 2007). MG leucocarbinol can diffuse rapidly into the cell membrane and has stronger toxicity, so it is necessary to carefully analyze the products of MG by LC-ESI-MS (Fig. 8). Analysis showed that product “a” at the m/z value of 329 is MG.

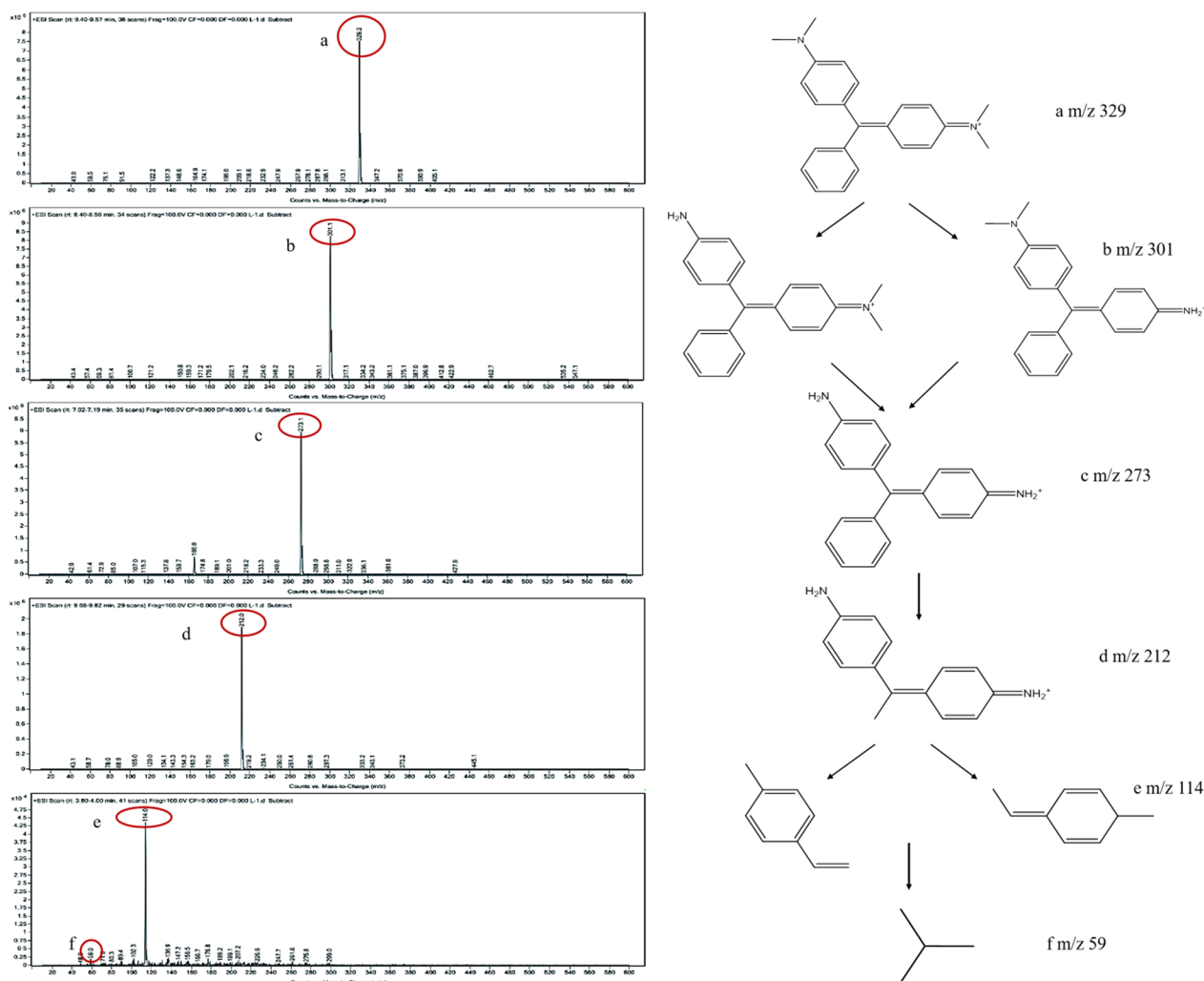


Fig. 8 LC-MS analysis of degradation pathway of MG by ZnO-Fe@SC

Product “b” (301) is the product “a” with two methyl groups removed, which contain two molecular formulae. Product “c” (273) is a result of undocking of the other two methyl groups, whereas product “d” (212) is result of the fracture of one benzene ring. Product “e” (114) contains two formulae due to the cleavage of the bond between the two benzene rings and the removal of one methyl group. The structure of the benzene ring has been destroyed in product “f” (59). Based on these intermediates, the possible photocatalytic degradation of MG by ZnO-Fe@SC is proposed. First, radicals generated by ZnO-Fe@SC, which were attacked the N, N-dimethyl position, induce the reactions such as demethylation and even deamination. But the chromophore structure is not destroyed. Then, radicals attack the central carbon, resulting in the decomposition of the conjugated structure. Finally, the benzene ring removal and ring opening reaction are carried out to degrade MG organic dye into small molecules.

3.8 Photocatalytic mechanism

The MG degradation experiments showed that photocatalytic performance of biochar-bimetallic photocatalyst was significantly better than that of biochar-semiconductor catalyst and bare semiconductor materials, which is consistent with previous studies (Yong et al. 2015). Based on the experimental results, the possible mechanism for the photodegradation of MG solution by ZnO-Fe@SC was deduced. ZnO-Fe@SC has larger specific surface area and abundant pores that can provide sufficient active reaction sites (BET) under dark reaction conditions. Under visible illumination, when the ZnO-Fe@SC heterostructure absorbs energy, the photo-generated electrons of Nano-ZnO easily and rapidly transfer to the CB of the surface of Fe@SC. This is based on the calculation result of E_{VB} and E_{CB} . Since *S. alterniflora* biochar has good electrical conductivity, the conduction band (CB) energy of Nano-ZnO is not sufficient to reduce O^2 to $\cdot O^{2-}$. This is because the CB potential of Nano-ZnO (-0.29 eV/vs. NHE) is lower than $E_0(O^2/\cdot O^{2-})$ (-0.33 eV/vs. NHE). The $\cdot O^{2-}$ is more likely to be generated on the surface of Fe@SC. The PL spectra showed that ZnO-Fe@SC had a lower e^-/h^+ charge carrier recombination rate. This indicates that the holes (h^+) leaving the valence band and the reduced $\cdot O^{2-}$ are the dominant active radicals, which is consistent with the radical scavenging experiment. Two kinds of active radicals, $\cdot O^{2-}$ and photoexcited holes (h^+), together degrade MG molecules in solution into small molecules by demethylation, deamination, destruction of the conjugated structure, removal of benzene ring and ring-opening reactions (LC-MS).

4 Conclusion

In summary, ZnO-Fe@SC heterostructure was successfully synthesized using the simultaneous magnetized carbonization method with the invasive alien species *S. alterniflora*, endowing its magnetic and photocatalytic properties, which is more energy-saving and high energy efficiency compared with the traditional two-step synthesis strategy. The prepared ZnO-Fe@SC exhibited high degradation efficiency for MG, which could reach up to 99.14% in 60 min, and could still maintain good performance after 5 cycles of use. ZnO-Fe@SC could degrade MG into small molecules by demethylation, deamination, and ring-opening reactions. The bimetals (Zn-Fe) of ZnO-Fe@SC endowed it with a heterogeneous structure, which could lower the recombination rate of charge carriers (e^-/h^+) and enhance the intensity of photogenerated electron transition, thus improving the photocatalytic activity. Therefore, ZnO-Fe@SC is an environmentally friendly, low-cost and highly efficient photocatalyst, which has enormous potential in the treatment of dye wastewater, and also provides new insights for high-value utilization of invasive species of plants such as *S. alterniflora*.

Supplementary Information

The online version contains supplementary material available at <https://doi.org/10.1007/s42773-023-00227-9>.

Additional file 1. Fig. S1. XPS spectrum of ZnO-Fe@SC. **Fig. S2.** N_2 adsorption-desorption isotherm. **Fig. S3.** UV-Vis absorption spectra of malachite green (MG) solution. **Fig. S4.** Active species trapping of ZnO-Fe@SC composite over MG (200 mg/L).

Acknowledgements

We would like to express our gratitude to the Zhejiang Jiaotou Mining Co. LTD for their sponsorship.

Author contribution

All authors contributed to the study conception and design. Material preparation, data collection and analysis were performed by JH. The first draft of the manuscript was written by JH and LJ. Resources, writing, reviewing and editing, visualization, supervision, project administration and funding acquisition were carried out by LJ and ZL. Investigation, data curation, software development was done by ZW. Validation, formal analysis, and investigation was performed by RL. Investigation and software development was done by KJ. All authors commented on previous versions of the manuscript, read and approved the final manuscript.

Funding

This work was supported by the Fundamental Research Funds for Zhejiang Provincial Universities and Research Institutes (No. 2021J004); the Scientific Research Fund of Zhejiang Provincial Education Department (No. Y202044721); and the Integration and demonstration project of key technologies for resource utilization of tuff stone powder and comprehensive treatment of contaminated soil (No. K20221027).

Availability of data and materials

The datasets used or analyzed during the current study are available from the corresponding author on reasonable request.

Declarations

Competing interests

The authors have no relevant financial or non-financial interests to disclose.

Author details

¹Ocean College, Zhejiang University, Zhoushan, Zhejiang 310058, China. ²National Marine Facilities Aquaculture Engineering Technology Research Center, Zhejiang Ocean University, Zhoushan, Zhejiang 316022, China. ³Zhejiang Lichen New Material Technology Co., Ltd, Shaoxing 313100, China.

Received: 28 December 2022 Revised: 24 April 2023 Accepted: 28 April 2023

Published online: 22 May 2023

References

- An S, Zhou GB, Wang C, Deng Z, Zhi Z, Li Y, Chen H, Yu L, Liu D (2007) *Spartina* invasion in China: implications for invasive species management and future research. *Weed Res* 47(3):183–191. <https://doi.org/10.1111/j.1365-3180.2007.00559.x>
- Bhavani P, Kumar D, Jeong S, Kim E, Park H, Hong S, Gopannagari M, Reddy D, Song J, Kim T (2018) Multidirectional-charge-transfer urchin-type Mo-doped $W_{18}O_{49}$ nanostructures on CdS Nanorods for enhanced photocatalytic hydrogen evolution. *Catal Sci Technol* 8:1880–1891. <https://doi.org/10.1039/C7CY02162C>
- Broadstock D, Ji Q, Managi S, Zhang D (2021) Pathways to carbon neutrality: challenges and opportunities. *Resour Conserv Recycl* 169:10547. <https://doi.org/10.1016/j.resconrec.2021.105472>
- Chahinez H, Abdelkader O, Leila Y, Tran H (2020) One-stage preparation of palm petiole-derived biochar: characterization and application for adsorption of crystal violet dye in water. *Environ Technol Innovation* 19:100872. <https://doi.org/10.1016/j.eti.2020.100872>
- Chen W, Parette R, Zou J, Cannon F, Dempsey B (2007) Arsenic removal by iron-modified activated carbon. *Water Res* 41(9):1851–1858. <https://doi.org/10.1016/j.watres.2007.01.052>
- Chen S, Hu Y, Meng S, Fu X (2014) Study on the separation mechanisms of photogenerated electrons and holes for composite photocatalysts $g-C_3N_4-WO_3$. *Appl Catal B* 150–151:564–573. <https://doi.org/10.1016/j.apcatb.2013.12.053>
- Du X, Li C, Zhao L, Zhang J, Gao L, Sheng J, Yi Y, Chen J, Zeng G (2018) Promotional removal of HCHO from simulated flue gas over Mn-Fe oxides modified activated coke. *Appl Catal B* 232:37–48. <https://doi.org/10.1016/j.apcatb.2018.03.034>
- Eltaweil A, Mohamed H, Monaem E, Subruiti G (2020) Mesoporous magnetic biochar composite for enhanced adsorption of malachite green dye: characterization, adsorption kinetics, thermodynamics and isotherms. *Adv Powder Technol* 31:1253–1263. <https://doi.org/10.1016/j.apt.2020.01.005>
- Harini K, Mohan C (2020) Isolation and characterization of micro and nanocrystalline cellulose fibers from the walnut shell, corncob and sugarcane bagasse. *Int J Biol Macromol* 163:1375–1383. <https://doi.org/10.1016/j.jbiomac.2020.07.239>
- Hedge P, Kriwoken L, Patten K (2003) A review of *Spartina* management in Washington State. *US J Aquat Plant Manage* 41:82–90
- Hosny M, Fawzy M, Eltaweil A (2022) Green synthesis of bimetallic Ag/ZnO@Biochar nanocomposite for photocatalytic degradation of tetracycline, antibacterial and antioxidant activities. *Sci Rep* 12:7316. <https://doi.org/10.1038/s41598-022-11014-0>
- Hu H, Sun L, Gao Y, Wang T, Huang Y, Lv C, Zhang Y, Huang Q, Chen X, Wu H (2020) Synthesis of ZnO nanoparticle-anchored biochar composites for the selective removal of perchlorate, a surrogate for pertechnetate, from radioactive effluents. *J Hazard Mater* 387:121670. <https://doi.org/10.1016/j.jhazmat.2019.121670>
- Huang D, Zhang Q, Zhang C, Wang R, Deng R, Luo H, Li T, Li J, Chen S, Liu C (2020) Mn-doped magnetic biochar as persulfate activator for the degradation of tetracycline. *Chem Eng J* 391(2020):123532. <https://doi.org/10.1016/j.cej.2019.123532>
- Jiang D, Liu X, Xu X, Zhang Y (2018) Double-shell Fe_3O_4 hollow box-like structure for enhanced photo-Fenton degradation of malachite green dye. *J Phys Chem Solids* 112:209–215. <https://doi.org/10.1016/j.jpjcs.2017.09.033>
- Kaliraj L, Ahn J, Rupa E, Abid S, Lu J, Yang D (2019) Synthesis of panos extract mediated ZnO Nano-flowers as photocatalyst for industrial dye degradation by UV illumination. *J Photochem Photobiol B* 199:111588. <https://doi.org/10.1016/j.jphotobiol.2019.111588>
- Kamal A, Saleem M, Alshaya H, Okla M, Chaudhary H, Munis M (2022) Ball-milled synthesis of maize biochar-ZnO nanocomposite (MB-ZnO) and estimation of its photocatalytic ability against different organic and inorganic pollutants. *J Saudi Chem Soc* 26(3):101445. <https://doi.org/10.1016/j.jscs.2022.101445>
- Karthik S, Siva P, Balu K, Suriyaprabha R, Rajendran V, Maaza M (2017) *Acalypha indica*-mediated green synthesis of ZnO Nanostructures under differential thermal treatment: Effect on textile coating, hydrophobicity, UV resistance, and antibacterial activity. *Adv Powder Technol* 28(12):3184–3194. <https://doi.org/10.1016/j.apt.2017.09.033>
- Kumar M, Suresh D, Sneharani A (2021) *Centella asiatica* mediated facile green synthesis of Nano zinc oxide and its photo-catalytic and biological properties. *Inorg Chem Commun* 133:108865. <https://doi.org/10.1016/j.inoche.2021.108865>
- Lawrinenko M, Laird D (2015) Anion exchange capacity of biochar. *Green Chem* 17(9):4628–4636. <https://doi.org/10.1039/C5CG00828J>
- Ledakowicz S, Paździor K (2021) Recent achievements in dyes removal focused on advanced oxidation processes integrated with Biological Methods. *Molecules* 26(4):870. <https://doi.org/10.3390/molecules26040870>
- Leichtweis J, Silvestri S, Carissimi E (2020) New composite of pecan nutshells biochar-ZnO for sequential removal of acid red 97 by adsorption and photocatalysis. *Biomass Bioenergy* 140:105648. <https://doi.org/10.1016/j.biombioe.2020.105648>
- Li H, Qu R, Li C, Guo W, Han X, He F, Ma Y, Xing B (2014) Selective removal of polycyclic aromatic hydrocarbons (PAHs) from soil washing effluents using biochars produced at different pyrolytic temperatures. *Bioresour Technol* 163:193–198. <https://doi.org/10.1016/j.biortech.2014.04.042>
- Li Y, Zhangqi G, Yuefei J, Xiaobin H, Cheng S, Shaogui Y, Lianhong W, Qingeng W, Die F (2015) Photodegradation of malachite green under simulated and natural irradiation: kinetics, products, and pathways. *J Hazard Mater* 285:127–136. <https://doi.org/10.1016/j.jhazmat.2014.11.041>
- Liang Q, Liu X, Wang J, Liu Y, Liu Z, Tang L, Shao B, Zhang W, Gong S, Cheng M, He Q, Feng C (2021) In-situ self-assembly construction of hollow tubular $g-C_3N_4$ isotype heterojunction for enhanced visible-light photocatalysis: experiments and theories. *J Hazard Mater* 401:123355. <https://doi.org/10.1016/j.jhazmat.2020.123355>
- Liu X, Li X, Liu X, He S, Jin J, Meng H (2019a) Green preparation of Ag-ZnO-rGO nanoparticles for efficient adsorption and photodegradation activity. *Colloids Surf A* 584:124011. <https://doi.org/10.1016/j.colsurfa.2019.124011>
- Liu S, Wang S, Jiang Y, Zhao Z, Jiang G, Sun Z (2019b) Synthesis of Fe_3O_4 loaded porous $g-C_3N_4$ photocatalyst for photocatalytic reduction of dinitrogen to ammonia. *Chem Eng J* 373:572–579. <https://doi.org/10.1016/j.cej.2019.05.021>
- Madhu R, Veeramani V, Chen S, Veerakumar P, Liu S, Miyamoto N (2016) Functional porous carbon-ZnO nanocomposites for high-performance biosensors and energy storage applications. *Phys Chem Chem Phys* 18(24):16466–16475. <https://doi.org/10.1039/C6CP01285J>
- Miao L, Shi B, Stanislaw N, Mu C, Qi K (2017) Facile synthesis of hierarchical ZnO microstructures with enhanced photocatalytic activity. *Mater Sci -Pol* 35(1):45–49. <https://doi.org/10.1515/msp-2017-0007>
- Naseer M, Aslam U, Khalid B, Chen B (2020) Green route to synthesize Zinc Oxide Nanoparticles using leaf extracts of *Cassia fistula* and *Melia azadirach* and their antibacterial potential. *Sci Rep* 10(1):1–10. <https://doi.org/10.1038/s41598-020-65949-3>
- Nidheesh P, Gopinath A, Ranjith N (2021) Potential role of biochar in advanced oxidation processes: a sustainable approach. *Chem Eng J* 405:126582. <https://doi.org/10.1016/j.cej.2020.126582>
- Niu Z, Feng W, Huang H, Wang B, Chen L, Miao Y, Su S (2020) Green synthesis of a novel Mn-Zn ferrite/biochar composite from waste batteries and pine sawdust for Pb^{2+} removal. *Chemosphere* 252:126529. <https://doi.org/10.1016/j.chemosphere.2020.126529>
- Noei H, Qiu H, Wang Y, Löffler E, Wöll C, Muhler M (2008) The identification of hydroxyl groups on ZnO nanoparticles by infrared spectroscopy. *Phys Chem Chem Phys* 10(47):7092–7097. <https://doi.org/10.1039/B811029H>

- Ouakouak A, Abdelhamid M, Thouraya B, Chahinez H, Hocine G, Hamdi N, Syafiuiddin A, Boopathy R (2021) Development of a Novel Adsorbent prepared from dredging sediment for effective removal of Dye in Aqueous Solutions. *Appl Sci* 11(22):10722. <https://doi.org/10.3390/app112210722>
- Otmane C, Ouakouak A, Touahra F, Grabi H, Martín J, Bilal M (2022) Date palm petiole-derived biochar: effect of pyrolysis temperature and adsorption properties of hazardous cationic dye from water. *Biomass Convers Biorefin* 1–11. <https://doi.org/10.1007/s13399-022-03127-3>
- Samadi M, Shivaee H, Zanetti M, Pourjavadi A, Moshfegh A (2012) Visible light photocatalytic activity of novel MWCNT-doped ZnO electrospun nanofibers. *J Mol Catal A: Chem* 359:42–48. <https://doi.org/10.1016/j.molcata.2012.03.019>
- Shao B, Liu X, Liu Z, Zeng G, Zhang W, Liang Q, Liu Y, He Q, Yuan X, Wang D, Luo S, Gong S (2019) Synthesis and characterization of 2D/0D g-C₃N₄/CdS-nitrogen doped hollow carbon spheres (NHCs) composites with enhanced visible light photodegradation activity for antibiotic. *Chem Eng J* 374:479–493. <https://doi.org/10.1016/j.cej.2019.05.202>
- Song J, Kim H, Jae W, Kim T, Futralan C, Kim J (2020) Porous ZnO/C microspheres prepared with maleopimaric acid as an anode material for lithium-ion batteries. *Carbon* 165:55–66. <https://doi.org/10.1016/j.carbon.2020.04.035>
- Tang L, Liu Y, Wang J, Zeng G, Deng Y, Dong H, Feng H, Wang J, Peng B (2018) Enhanced activation process of persulfate by mesoporous carbon for degradation of aqueous organic pollutants: electron transfer mechanism. *Appl Catal B* 231:1–10. <https://doi.org/10.1016/j.apcatb.2018.02.059>
- Thi T, Nguyen T, Thi Y, Thi K, Phan B, Pham K (2020) Green synthesis of ZnO nanoparticles using orange fruit peel extract for antibacterial activities. *RSC Adv* 10(40):23899–23907. <https://doi.org/10.1039/D0RA04926C>
- Wan Z, Wang J (2017) Degradation of sulfamethazine using Fe₃O₄-Mn₃O₄/reduced graphene oxide hybrid as Fenton-like catalyst. *J Hazard Mater* 324:653–664. <https://doi.org/10.1016/j.jhazmat.2016.11.039>
- Yan W, Zhang R, Ji F, Jing C (2020) Deciphering co-catalytic mechanisms of potassium doped g-C₃N₄ in Fenton process. *J Hazard Mater* 392:122472. <https://doi.org/10.1016/j.jhazmat.2020.122472>
- Yang T, Xu Y, Huang Q, Sun Y, Liang X, Wang L, Qin X, Zhao L (2021) Adsorption characteristics and the removal mechanism of two novel Fe-Zn composite modified biochar for Cd(II) in water. *Bioresour Technol* 333:125078. <https://doi.org/10.1016/j.biortech.2021.125078>
- Yao Y, Lu F, Zhu Y, Wei F, Liu X, Lian C, Wang S (2015) Magnetic core-shell CuFe₂O₄@C₃N₄ hybrids for visible light photocatalysis of Orange II. *J Hazard Mater* 297:224–233. <https://doi.org/10.1016/j.jhazmat.2015.04.046>
- Yao Y, Hu H, Zheng H, Hu H, Tang Y, Liu X, Wang S (2022) Nonprecious bimetallic Fe, Mo-embedded N-enriched porous biochar for efficient oxidation of aqueous organic contaminants. *J Hazard Mater* 422:126776. <https://doi.org/10.1016/j.jhazmat.2021.126776>
- Yong L, Zhangqi G, Yuefei J, Xiaobin H, Cheng S, Shaogui Y, Lianhong W, Qingeng W, Die F (2015) Photodegradation of malachite green under simulated and natural irradiation: Kinetics, products, and pathways. *J Hazard Mater* 285:127–136. <https://doi.org/10.1016/j.jhazmat.2014.11.041>
- Yu Y, An Q, Jin L, Luo N, Li Z, Jiang J (2020) Unraveling sorption of Cr(VI) from aqueous solution by FeCl₃ and ZnCl₂-modified corn stalks biochar: implicit mechanism and application. *Bioresour Technol* 297:122466. <https://doi.org/10.1016/j.biortech.2019.122466>
- Zhang C, Li F, Wen R, Zhang H, Elumalai P, Zheng Q, Chen H, Yang Y, Huang M, Ying G (2020a) Heterogeneous electro-Fenton using three-dimension NZVI-BC electrodes for degradation of neonicotinoid wastewater. *Water Res* 182:115975. <https://doi.org/10.1016/j.watres.2020.115975>
- Zhang Y, Su P, Weathersby D, Zhang Q, Zheng J, Fan R, Zhang J, Dai Q (2020b) Synthesis of γ-Fe₂O₃-ZnO-biochar nanocomposites for rhodamine B removal. *Appl Surf Sci* 501:144217. <https://doi.org/10.1016/j.apsusc.2019.144217>
- Zubrik A, Matik M, Mačingová E, Danková Z, Jáger D, Briančin J, Machala L, Pechoušek J, Hredzák S (2022) The use of microwave irradiation for preparation and fast-acting regeneration of magnetic biochars. *Chem Eng Process* 178:109016. <https://doi.org/10.1016/j.cep.2022.109016>

Submit your manuscript to a SpringerOpen[®] journal and benefit from:

- Convenient online submission
- Rigorous peer review
- Open access: articles freely available online
- High visibility within the field
- Retaining the copyright to your article

Submit your next manuscript at ► [springeropen.com](https://www.springeropen.com)